Voltage-driven gigahertz frequency tuning of spin Hall nano-oscillators

Jong-Guk Choi
KAIST
Jaehyeon Park
KAIST
Min-Gu Kang
Korea Advanced Institute of Science and Technology
Doyoon Kim
Korea University
Jae-Sung Rieh
Korea University
Kyung-Jin Lee
Korea Advanced Institute of Science and Technology (KAIST) https://orcid.org/0000-0001-6269-2266
Kab-Jin Kim
Korea Advanced Institute of Science and Technology https://orcid.org/0000-0002-8378-3746
Byong-Guk Park (bgpark@kaist.ac.kr)
KAIST https://orcid.org/0000-0001-8813-7025

Article

Keywords: Spin Hall nano-oscillators, oscillator-based neuromorphic computing, oscillation frequency

Posted Date: September 8th, 2021

DOI: https://doi.org/10.21203/rs.3.rs-840717/v1

Version of Record: A version of this preprint was published at Nature Communications on June 30th, 2022. See the published version at https://doi.org/10.1038/s41467-022-31493-z.

Voltage-driven gigahertz frequency tuning of spin Hall nano-oscillators

Jong-Guk Choi[1†], Jaehyeon Park[2†], Min-Gu Kang[1], Doyoon Kim[3], Jae-Sung Rieh[3], Kyung-Jin Lee[2], Kab-Jin Kim[2★] and Byong-Guk Park[1★]

[1] *Department of Materials Science and Engineering, KAIST, Daejeon 34141, Korea*

[2] *Department of Physics, KAIST, Daejeon 34141, Korea*

[3] *School of Electrical Engineering, Korea University, Seoul 02841, Korea*

† *These two authors equally contributed to this work.*

★ **Correspondence to:** kabjin@kaist.ac.kr (K.-J.K.) and bgpark@kaist.ac.kr (B.-G.P.)

Abstract

Spin Hall nano-oscillators (SHNOs) exploiting current-driven magnetization auto-oscillation have recently received much attention because of their potential for oscillator-based neuromorphic computing. Widespread neuromorphic application with SHNOs requires an energy-efficient way to tune oscillation frequency in broad ranges and store trained frequencies in SHNOs without the need for additional memory circuitry. Voltage control of oscillation frequency of SHNOs was experimentally demonstrated, but the voltage-driven frequency tuning was volatile and limited to megahertz ranges. Here, we show that the frequency of SHNO is controlled up to 2.1 GHz by a moderate electric field of 1.25 MV/cm. The large frequency tuning is attributed to the voltage-controlled magnetic anisotropy (VCMA) in a perpendicularly magnetized Ta/Pt/$[Co/Ni]_n$/Co/AlO_x structure. Moreover, non-volatile VCMA effect enables control of the cumulative

frequency using repetitive voltage pulses, which mimic the potentiation and depression functions of biological synapses. Our results suggest that the voltage-driven frequency tuning of SHNOs facilitates the development of energy-efficient spin-based neuromorphic devices.

Spintronic oscillators that generate microwaves through spin-torque-driven magnetization precession are being extensively investigated for neuromorphic applications [1-4] owing to their unique features such as non-linearity [5,6], low-power operation [7,8], scalability [1,4,9], and CMOS compatibility [10]. Indeed, spin-transfer-torque-based oscillators (STOs) have recently been implemented in oscillator neural networks, demonstrating pattern recognition [2,11,12]. Furthermore, the STO device has been successfully trained to recognize the input pattern signals by tuning the frequency of individual oscillators using a driving current [2,11] or magnetic field [12]. However, the current or magnetic field-based frequency tuning is not energy efficient; thus, it is necessary to find an alternative way to tune the frequency widely with reduced power consumption.

Recently, another type of STO, in which magnetization precession is caused by spin currents generated by the spin Hall effect [13-15], has been developed, which is referred to as spin Hall nano-oscillator (SHNO) [16-20]. Since the SHNO is operated with an in-plane current, it has the following advantages over conventional STO that utilizes a perpendicular current. First, multiple oscillators integrated into a common spin-Hall material can be controlled simultaneously by an in-plane current, allowing long-range mutual synchronization of the SHNOs [21,22]. Second, a gate structure is easily incorporated in a three-terminal SHNO structure [23-25], so that an individual oscillator can be independently controlled by a gate voltage [26,27].

A recent study [27] has experimentally demonstrated the gate voltage-induced frequency tuning in W/CoFeB/MgO structures with the frequency tuning range of about 50 MHz. However, this frequency tuning range is relatively narrow compared to the oscillation frequency (~ 10 GHz). Thus, although 10~50 MHz frequency tunability is sufficient to optimize the synchronization map for a small number of different synchronization states as in

vowel recognition [2,27], a wider frequency tunability is required for tasks having more states of being recognized and thus expands the applicability of gate-controlled SHNOs to widespread oscillator-based neuromorphic computing. Moreover, the previously demonstrated voltage-driven frequency tuning of SHNO [27] is volatile, so that an additional memory circuitry is required to store trained synaptic weights of oscillation frequency.

In this Article, we report voltage-driven large frequency tuning of SHNO by exploiting voltage-controlled magnetic anisotropy (VCMA) [28-33] as schematically illustrated in Fig. 1a. The SHNO consists of a ferromagnet (FM)/heavy metal (HM) bilayer. In this geometry, a charge current flowing through the HM layer generates a vertical spin current via the spin Hall effect, which exerts spin-orbit torques (SOTs) on the magnetization of the FM layer. The auto-oscillation of magnetization occurs when the SOT (green arrow) fully compensates the damping torque (gray arrow), and the auto-oscillation frequency is governed by the resonance frequency (f_{res}) of the ferromagnet. Here, we employ a perpendicular magnetic anisotropy (PMA) material, which is distinct from previous works where in-plane magnetized materials were generally used. In the presence of an in-plane field, f_{res} of a PMA material is determined as [34-36],

$$f_{\mathrm{res}} = \frac{\gamma}{2\pi}\sqrt{B_{\mathrm{k}}^2 - {B_{\parallel}}^2}\ (0 < B_{\parallel} < B_{\mathrm{k}}),$$

$$f_{\mathrm{res}} = \frac{\gamma}{2\pi}\sqrt{B_{\parallel}(B_{\parallel} - B_{\mathrm{k}})}\ (B_{\parallel} \geq B_{\mathrm{k}}), \qquad (1)$$

where γ is the gyromagnetic ratio, B_{k} is the effective perpendicular anisotropy field, and $B_{\parallel}$ is the external in-plane magnetic field. Equation (1) indicates that a broad frequency tuning is effectively achieved by controlling B_{k}. Figure 1b shows an example; when $B_{\parallel}$ is larger than B_{k}, the frequency increases by weakening B_{k}. In this work, we demonstrate that B_{k} of

perpendicularly magnetized Co/Ni multilayers is controlled as large as 0.22 T by a moderate electric field of 1.25 MV/cm. This results in a frequency tuning up to 2.1 GHz, which is more than 40 times larger than the previously reported values [26,27]. We find that the voltage-controlled frequency tuning is independent of the driving current and is much more efficient than the current-controlled frequency tuning used in conventional STOs. Furthermore, the voltage effect is non-volatile in our sample, allowing the cumulative frequency control of SHNO using repetitive voltage pulses. This can facilitate the potentiation and depression functions of artificial synapses [37-40], and thus can be utilized in the learning process of neuromorphic devices. Our results demonstrating efficient frequency tuning of SHNO via gate voltage provide an essential building block for spin-based low power neuromorphic hardware applications.

Voltage-controlled perpendicular magnetic anisotropy

We first demonstrate the VCMA effect in a Co/Ni multilayer sample of Ta (3 nm)/Pt (5 nm)/[Co (0.45 nm)/Ni (0.6 nm)]$_7$/Co (0.45 nm)/AlO_x (2 nm) structures (see Methods for details of sample growth). Figure 1c shows the magnetization measurement while sweeping a perpendicular magnetic field (B_z), indicating that the Co/Ni film has PMA. To test the VCMA of the sample, we patterned the film into a Hall bar device with a 10 μm × 10 μm cross, which is fully covered by a gate oxide of ZrO_2 (40 nm) and a gate electrode of Ru (50 nm). Figure 1d shows the anomalous Hall resistance (R_H) after sequentially applying a gate voltage (V_g). Here, we applied a V_g to the top electrode for 5 minutes at 150 ℃ and then measured R_H at room temperature. This is possible because the voltage effect is maintained even after turning off the V_g [31,32,41,42]. The result shows that the PMA is gradually weakened by positive V_g's and

restored by subsequent negative V_g's, indicating that the PMA in our Co/Ni multilayer sample is effectively modulated by V_g. Note that the V_g of 5 V is equivalent to an electric field of 1.25 MV/cm.

In order to quantitatively analyze the VCMA effect, we performed the spin torque-ferromagnetic resonance (ST-FMR) measurement. The ST-FMR spectra were measured using a bar-shaped device (8 μm × 14 μm) fabricated from the same Co/Ni film. The microwave frequency used for the ST-FMR measurement ranges from 10 GHz to 21 GHz (see Methods for measurement details). Figure 2a shows the ST-FMR spectra of the sample with different V_g's at a frequency of 15 GHz, measured while sweeping magnetic fields in a direction slightly tilted from the z-direction. The ST-FMR spectra can be expressed by the combination of symmetric and anti-symmetric Lorentzian functions as [43,44],

$$V_{\mathrm{ST-FMR}}(B_z) = V_{\mathrm{sym}} \frac{\Delta B^2}{(B_z - B_{\mathrm{res,z}})^2 + \Delta B^2} + V_{\mathrm{asy}} \frac{\Delta B (B_z - B_{\mathrm{res,z}})}{(B_z - B_{\mathrm{res,z}})^2 + \Delta B^2}, \quad (2)$$

where $B_{\mathrm{res,z}}$ is the center magnetic field of the Lorentzian functions corresponding to the resonance magnetic field, ΔB is the linewidth (half-width at half maximum) of the Lorentzian function, and $V_{\mathrm{sym}}(V_{\mathrm{asy}})$ is a symmetric (anti-symmetric) component of resonance amplitude. The dotted lines represent the fitting curves of the ST-FMR spectra using Eq. (2), from which we extracted the $B_{\mathrm{res,z}}$ and ΔB values. It is observed that the Lorentzian curve for the initial sample (black symbols) is centered around 0.34 T. That is, $B_{\mathrm{res,z}}$ = 0.34 T. Notably, the $B_{\mathrm{res,z}}$ is largely shifted by the V_g; the $B_{\mathrm{res,z}}$ is increased up to 0.59 T by a positive voltage (+5 V, red symbols), but it is then reduced to 0.39 T by a subsequent negative voltage (-5 V, blue symbols). We measured the $B_{\mathrm{res,z}}$ for different frequencies (see Supplementary Note 1) and summarize the resonance frequency $f_{\mathrm{res,z}}$ vs $B_{\mathrm{res,z}}$ in Fig. 2b, where the black symbols represent the initial

sample without applying a V_g, while the red and blue symbols correspond to the samples after successively applying +5 V and -5 V, respectively. The linear relation between the $f_{res,z}$ and $B_{res,z}$ is well explained by the Kittel formula $f_{res,z} = \frac{\gamma}{2\pi}(B_{res,z} + B_k)$ [45], from which the B_k can be extracted. We note that the ST-FMR measurement was done under a magnetic field along the *z*-direction, so the above resonance frequency formula is different from Eq. (1), which is based on an in-plane magnetic field. Figure 2c shows the extracted B_k according to the V_g; the B_k reduces from 0.16±0.01 T to -0.08±0.01 T when applying +5 V, and is restored close to the initial value by a negative gate of -5 V. This is consistent with the results shown in Fig. 1c. Note that the average change of B_k is 0.22±0.02 T by ±5 V, which can cause a frequency tuning up to a few GHz according to Eq. (1).

Figure 2d shows the ΔB as a function of $f_{res,z}$, where the color symbols represent the samples with different V_g's, identical to those in Fig. 2b. Using the relation $\Delta B = \Delta B_0 + \frac{2\pi\alpha_{eff}}{\gamma} f_{res,z}$ [43-46], the effective magnetic damping constant α_{eff} is obtained. Here, ΔB_0 is the zero-frequency linewidth due to long-range magnetic inhomogeneity [46]. Figure 2f shows the dependence of the α_{eff} on V_g; the α_{eff} decreases (increases) by a positive (negative) V_g. This is consistent with the previous reports [27], where the voltage-driven frequency tuning was obtained in the MHz range. The possible effect of the voltage-controlled α_{eff} on the frequency tuning in our sample will be discussed later.

Voltage-driven frequency tuning of SHNO

We now move on to our main result, i.e., the gate voltage-induced frequency tuning of SHNO.

Figure 3a illustrates the measurement schematics; the SHNO device was fabricated by patterning the Co/Ni film into a nano-constriction with a width of 140 nm, which is entirely covered by a gate oxide of ZrO_2 (40 nm) and a gate electrode of Ru (50 nm). A dc current (I_{dc}) is applied along the constriction channel (x-direction) under a magnetic field (B) applied in the direction with a polar angle θ of 80° and an azimuthal angle φ of 70°. In this geometry, the I_{dc} generates SOTs through the spin Hall effect in the Pt underlayer, which leads to a magnetization oscillation of the Co/Ni layer when the SOT compensates the damping torque. The magnetization oscillation causes a periodic change in magnetoresistance (MR) of the same frequency [10], which is detected by a power spectral density (PSD) (see Methods for more details of measurement). To check whether the MR of the nano-constricted device is large enough to generate a detectable PSD, we measured the MR of the nano-constriction sample using an in-plane rotating magnetic field of 1 T (Fig. 3b). The MR ratio is about 1.2 %, which is sufficient to monitor the auto-oscillation of magnetization [17-19].

Figure 3c shows the color plots of PSD as a function of a magnetic field (B) for the initial sample without applying a V_g. Here, we used a fixed I_{dc} of 2.9 mA. The auto-oscillation peak is clearly visible, and the peak frequency increases with the increasing magnetic field, demonstrating that our Co/Ni device successfully operates as an SHNO. We then investigate the effect of V_g on the auto-oscillation. The V_g was applied in the same manner as the R_H measurement as shown in Fig. 1. Figures 3d-3g show the results, where V_g's of +4 V, +5 V, -2 V, and -3 V were successively applied. Notably, the auto-oscillation frequency is vertically shifted by V_g's; it increases (decreases) by a positive (negative) V_g. This is consistent with our expectation as illustrated in Fig. 1a, i.e., a positive (negative) V_g reduces (enhances) PMA or B_k and consequently increases (decreases) the oscillation frequency. To clearly visualize the

gate voltage-induced frequency tuning, we extract the auto-oscillation spectra for $B = 0.52\ T$ from Figs. 3c-3g and plot them in Fig. 3h. This demonstrates that the amount of the frequency tuning is up to 2.1 GHz with a V_g of 5 V, which is remarkably larger than the previously reported value of 50 MHz [26,27] with a similar V_g. This wider frequency tunability allows more states to be recognized, expanding the applicability to a wide range of oscillator-based neuromorphic computing. Note that similar results are observed in another Co/Ni device with a different thickness (Supplementary Note 2), confirming the reproducibility of the voltage-controlled frequency tuning of the SHNO.

We next investigate the current dependent auto-oscillation of the SHNO. Figures 4a-4e show PSD spectra as a function of current for the sample with different V_g's. Here, we used a fixed magnetic field of 0.52 T. It is found that the application of the V_g changes two properties of the SHNO: auto-oscillation frequency and threshold current (I_{th}) at which auto-oscillation begins to occur. First, the auto-oscillation peaks shift up and down according to the V_g, demonstrating the voltage-controlled frequency tuning, consistent with the results shown in Fig. 3. Note that the oscillation frequency slightly increases with increasing I_{dc}, which is attributed to the increase in SOT [6,24,26,47]. However, the maximum frequency tuning by a current within this measurement range is ~0.26 GHz, which is much smaller than that by V_g (~2.1 GHz). Furthermore, the slope of the oscillation frequency with respect to I_{dc} is independent of the V_g, demonstrating that the current-induced SOT is not significantly affected by the V_g. This is confirmed by in-plane harmonic Hall measurements (Supplementary Note 3) [49]. Second, the I_{th} is also modified by the V_g. Figure 4f shows the I_{th} according to the V_g. Here, the I_{th} values are extracted by a linear fit of the inverse of the PSD integral (Supplementary Note 4) [48]. The I_{th} decreases (increases) for positive (negative) V_g's. Since the auto-oscillation occurs

when SOT compensates magnetic damping torque, the voltage-dependent I_{th} is attributed to the voltage controlled α_{eff} [6,24,47,50] as shown in Fig. 2e. Another interesting point is that the VCMA effect of the sample is non-volatile, so is the voltage-controlled frequency tuning; the auto-oscillation frequency is maintained even after the V_{g} is turned off. This is distinct from the previous work, in which the frequency tuning only occurs during gate application.

Cumulative frequency control via a repetitive voltage pulse

We finally demonstrate the emulation of synaptic plasticity [37-40], a key function in the learning process of neuromorphic devices, by exploiting the non-volatility of our voltage-controlled SHNO. For this experiment, we fabricated a 100-nm-width constriction SHNO device with a Ta (3 nm)/Pt (5 nm)/[Co (0.4 nm)/Ni (0.6 nm)]$_7$/Co (0.4 nm)/AlO_x (2 nm) structure. To verify the cumulative frequency tuning, we applied a series of voltage pulses and measured the auto-oscillation spectrum between the pulses under a magnetic field (B) of 0.9 T applied in the direction with a polar angle θ of 80° and an azimuthal angle φ of 70°. Here, a V_{g} of 10 seconds was applied at room temperature while applying a current of 1.8 mA, different from the experiments shown in Figs. 2-4, where a V_{g} was applied at 150°C. Figure 5a shows the frequency change with the number of V_{g} pulses ($N_{V_{\mathrm{g}}}$) of ±6 V. The oscillation frequency gradually increases by about 1.24 GHz as the number of V_{g} pulses of +6 V increase, and it is then restored to its initial value by subsequent negative V_{g} pulses of -6 V. The frequency tuning for successive positive and negative voltage pulses mimics the synaptic potentiation (strengthening in synaptic weight) and depression (weakening of synaptic weight), respectively. Figure 5b shows the cumulative frequency change (δf) for various V_{g} amplitudes,

demonstrating that the frequency change rate ($\delta f / N_{V_g}$) is effectively tuned by the magnitude of the V_g. The voltage dependence of the frequency change rate can emulate the stimulus-dependent synaptic transition rate in a neuromorphic device. Furthermore, our device memorizes the modulated frequency with its non-volatile nature, offering a compact device layout that can store trained synaptic weights without the need for a separate memory circuitry required for conventional STOs [2,11].

Conclusion

We have demonstrated the voltage-driven GHz frequency tuning of SHNO with perpendicularly magnetized Pt/$[Co/Ni]_n$/Co/AlO_x structures. It is found that the auto-oscillation frequency of the SHNO is effectively modulated up to 2.1 GHz by controlling the PMA with a V_g of 5 V, which is equivalent to 1.25 MV/cm. This demonstrates that voltage-driven frequency tuning is much more efficient than conventional current- (or magnetic field-) controlled frequency tuning. Moreover, owing to the non-volatile nature of the gate effect, the cumulative oscillation frequency is controlled by repetitive voltage pulses, which can mimic the biological synaptic functions of stimulus-dependent potentiation and depression. Therefore, our SHNO device can be utilized in the learning process of neuromorphic devices, and thereby facilitates spin-based low power neuromorphic hardware applications.

Methods

Sample preparation. The thin films of Ta/Pt/$[Co/Ni]_n$/Co/AlO_x structures were fabricated on high resistivity Si substrates by magnetron sputtering under a base pressure of 4.0×10^{-6} Pa at room temperature. The metallic layers were deposited with an Ar gas pressure of 0.4 Pa and a dc power of 30 W, and the AlO_x layer was formed by plasma oxidation of an Al layer with an O_2 pressure of 4.0 Pa and a dc power of 30 W for 75 s. The ZrO_2 gate oxide (40 nm) was grown at 125 ℃ by plasma-enhanced atomic layer deposition (PE-ALD) using a TEMAZ [Tetrakis(ethylmethylamido)zirconium] precursor. The oxygen plasma for the PE-ALD was formed with an rf power of 60 W and an O_2 gas flow of 500 sccm.

Power spectral density (PSD) measurement. All PSD measurements were carried out at room temperature using a home-built probe station, where the sample was placed on an angle controllable holder located between two poles of an electromagnet. We used a bias-T to inject a dc current and to detect microwave signals simultaneously. A dc current was applied to the sample using a current source (Keithley 2450) with a current compliance of 3 mA that prevents the sample degradation. The microwave signal generated from the sample was amplified by a low-noise amplifier (gain of +45 dB) and detected by a spectrum analyzer (Keysight N5173B). The resolution bandwidth and video bandwidth were set to 2 MHz and 9 kHz, respectively. The measured spectra were averaged at least 3 times to increase the signal-to-noise ratio.

Spin torque ferromagnetic resonance (ST-FMR) measurement. ST-FMR measurements were performed at room temperature using the same probe station used in PSD measurement. For the ST-FMR measurement, we applied a magnetic field in the direction slightly tilted from the *z*-axis to attain an FMR rectified voltage. A microwave signal (power of +14 dBm) was injected into the sample by a signal generator (Keysight N9000B) through the RF port of a

bias-T, and a dc voltage generated from the sample was detected by a lock-in amplifier (SRS SR830). The tuning frequency was set to 313 Hz.

References

1. Torrejon, J. et al. Neuromorphic computing with nanoscale spintronic oscillators. *Nature* **547**, 428–431 (2017).

2. Romera, M. et al. Vowel recognition with four coupled spin-torque nano-oscillators. *Nature* **563**, 230–234 (2018)

3. Riou, M. et al. Temporal Pattern Recognition with Delayed-Feedback Spin-Torque Nano-Oscillators. *Phys. Rev. Appl*. **12**, 024049 (2019).

4. Grollier, J., Querlioz, D. & Stiles, M. D. Spintronic Nanodevices for Bioinspired Computing. *Proc. IEEE* **104**, 2024–2039 (2016).

5. Slavin, A. & Tiberkevich, V. Nonlinear auto-oscillator theory of microwave generation by spin-polarized current. *IEEE Trans. Magn.* **45**, 1875–1918 (2009).

6. Kim, J., Tiberkevich, V. & Slavin, A. Generation Linewidth of an Auto-Oscillator with a Nonlinear Frequency Shift: Spin-Torque Nano-Oscillator. *Phys. Rev. Lett.* **100**, 017207 (2008).

7. Locatelli, N., Cros, V. & Grollier, J. Spin-torque building blocks. *Nat. Mater.* **13**, 11–20 (2014).

8. Lee, H. S. et al. Power-efficient spin-torque nano-oscillator-based wireless communication with CMOS high-gain low-noise transmitter and receiver. *IEEE Trans. Magn*. **55**, 4001910 (2019).

9. Das, D., Tulapurkar, A. & Muralidharan, B. Scaling Projections on Spin-Transfer Torque Magnetic Tunnel Junctions. *IEEE Trans. Electron Devices* **65**, 724–732 (2018).

10. Chen, T. et al. Spin-Torque and Spin-Hall Nano-oscillators. *Proc. IEEE* **104**, 1919-1945 (2016).

11. Vodenicarevic, D., Locatelli, N., Abreu Araujo, F., Grollier, J. & Querlioz, D. A Nanotechnology-Ready Computing Scheme based on a Weakly Coupled Oscillator Network. *Sci. Rep*. 7, 44772 (2017).

12. Yogendra, K., Fan, D., Jung, B. & Roy, K. Magnetic Pattern Recognition Using Injection-

Locked Spin-Torque Nano-Oscillators. *IEEE Trans. Electron Devices* **63**, 1674–1680 (2016).

13. Hirsch, J. E. Spin Hall Effect. *Phys. Rev. Lett.* **83**, 1834-1837 (1999).

14. Kato, Y. K., Myers, R. C., Gossard, A. C. & Awschalom, D. D. Observation of the spin Hall effect in semiconductors. *Science* **306**, 1910–1913 (2004).

15. Sinova, J., Valenzuela, S. O., Wunderlich, J., Back, C. H. & Jungwirth, T. Spin Hall effects. *Rev. Mod. Phys.* **87**, 1213–1260 (2015).

16. Demidov, V. E. et al. Magnetic nano-oscillator driven by pure spin current. *Nat. Mater.* **11**, 1028–1031 (2012).

17. Liu, R. H., Lim, W. L. & Urazhdin, S. Spectral characteristics of the microwave emission by the spin hall nano-oscillator. *Phys. Rev. Lett.* **110**, 147601 (2013).

18. Demidov, V. E., Urazhdin, S., Zholud, A., Sadovnikov, A. V. & Demokritov, S. O. Nanoconstriction-based spin-Hall nano-oscillator. *Appl. Phys. Lett.* **105**, (2014).

19. Duan, Z. et al. Nanowire spin torque oscillator driven by spin orbit torques. *Nat. Commun.* 5, 5616 (2014).

20. Dürrenfeld, P., Awad, A. A., Houshang, A., Dumas, R. K. & Åkerman, J. A 20 nm spin Hall nano-oscillator. *Nanoscale* **9**, 1285–1291 (2017).

21. Awad, A. A. et al. Long-range mutual synchronization of spin Hall nano-oscillators. *Nat. Phys.* **13**, 292–299 (2017).

22. Zahedinejad, M. et al. Two-dimensional mutually synchronized spin Hall nano-oscillator arrays for neuromorphic computing. *Nat. Nanotechnol.* **15**, 47–52 (2020).

23. Liu, L., Pai, C. F., Ralph, D. C. & Buhrman, R. A. Magnetic oscillations driven by the spin Hall effect in 3-terminal magnetic tunnel junction devices. *Phys. Rev. Lett.* **109**, 186602 (2012).

24. Tarequzzaman, M. et al. Spin torque nano-oscillator driven by combined spin injection from tunneling and spin Hall current. *Commun. Phys*. **2**, 20 (2019).

25. Albertsson. D. I., Zahedinejad, M., Åkerman, J., Rodriguez, S. & Rusu, A. Compact

Macrospin-Based Model of Three-Terminal Spin-Hall Nano Oscillators. *IEEE Trans. Magn*. **55**, 4003808 (2019).

26. Liu, R. H., Chen, L., Urazhdin, S. & Du, Y. W. Controlling the spectral characteristics of a spin-current auto-oscillator with an electric field. *Phys. Rev. Appl*. **8**, 021001 (2017).

27. Fulara, H. et al. Giant voltage-controlled modulation of spin Hall nano-oscillator damping. *Nat. Commun.* **11**, 4006 (2020).

28. Ohno, H. et al. Electric-field control of ferromagnetism. *Nature* **408**, 944–946 (2000).

29. Maruyama, T. et al. Large voltage-induced magnetic anisotropy change in a few atomic layers of iron. *Nat. Nanotechnol*. **4**, 158–161 (2009).

30. Nakamura, K. et al. Giant modification of the magnetocrystalline anisotropy in transition-metal monolayers by an external electric field. *Phys. Rev. Lett.* **102**, 187201 (2009).

31. Bi, C. et al. Reversible control of Co magnetism by voltage-induced oxidation. *Phys. Rev. Lett.* **113**, 267202 (2014).

32. Bauer, U. et al. Magneto-ionic control of interfacial magnetism. *Nat. Mater.* **14**, 174–181 (2015).

33. Weisheit, M. et al. Electric Field–Induced Modification of Magnetism in Thin-Film Ferromagnets. *Science* **315**, 349-351 (2007).

34. Kittel, C. On the theory of ferromagnetic resonance absorption. *Phys. Rev.* **73**, 155 (1948).

35. Farle, M. Ferromagnetic resonance of ultrathin metallic layers. *Rep. Prog. Phys.* **61**, 755-826 (2018)

36. He, C. et al. Spin-Torque Ferromagnetic Resonance in W/Co-Fe-B/W/Co-Fe-B/MgO Stacks. *Phys. Rev. Appl*. **10**, 034067 (2018).

37. Ho, V. M., Lee, J.-A. & Martin, K. C. The cell biology of synaptic plasticity. *Science* **334**, 623–628 (2011).

38. Jo, S. H. et al. Nanoscale memristor device as synapse in neuromorphic systems. *Nano Lett.* **10**, 1297–1301 (2010).

39. Mishra, R., Kumar, D. & Yang, H. Oxygen-Migration-Based Spintronic Device Emulating

a Biological Synapse. *Phys. Rev. Appl.* **11**, 054065 (2019).

40. Huang, W. et al. Memristive Artificial Synapses for Neuromorphic Computing. *Nano-Micro Lett.* **13**, 85 (2021).

41. Baek, S.-H. C. et al. Complementary logic operation based on electric-field controlled spin-orbit torques. *Nat. Electron.* **1**, 398–403 (2018).

42. Park, K.-W. et al. Electric field control of magnetic anisotropy in the easy cone state of Ta/Pt/CoFeB/MgO structures. *Appl. Phys. Lett.* **109**, 012405 (2016).

43. Liu, L., Moriyama, T., Ralph, D. C. & Buhrman, R. A. Spin-torque ferromagnetic resonance induced by the spin Hall effect. *Phys. Rev. Lett.* **106**, 306601 (2011).

44. Kim, J. et al. Spin-orbit torques associated with ferrimagnetic order in Pt/GdFeCo/MgO layers. *Sci. Rep.* **8**, 6017 (2018).

45. Beaujour, J.-M., Ravelosona, D., Tudosa, I., Fullerton, E. E. & Kent, A. D. Ferromagnetic resonance linewidth in ultrathin films with perpendicular magnetic anisotropy. *Phys. Rev. B* **80**, 180415(R) (2009).

46. McMichael, R. D., Twisselmann, D. J. & Kunz, A. Localized Ferromagnetic Resonance in Inhomogeneous Thin Films. *Phys. Rev. Lett.* **90**, 227601 (2003).

47. Slonczewski, J. C., Current-driven excitation of magnetic multilayers. J. Magn. Magn. Mater. **159**, L1-L7 (1996)

48. Zheng, C., Chen, H. H., Zhang, X., Zhang, Z. & Liu, Y. Spin torque nano-oscillators with a perpendicular spin polarizer. *Chinese Phys. B* **28**, (2019).

49. Hayashi, M., Kim, J., Yamanouchi, M. & Ohno, H. Quantitative characterization of the spin-orbit torque using harmonic Hall voltage measurements. *Phys. Rev. B* **89**, 144425 (2014).

50. Rippard, W. H. et al. Spin-transfer dynamics in spin valves with out-of-plane magnetized CoNi free layers. *Phys. Rev. B* **81**, 014426 (2010).

Acknowledgments

This work is supported by the Samsung Research Funding Center of Samsung Electronics under Project Numbers SRFC-MA1702-02 and SRFC-MA1802-01. K.-J.K acknowledges support from KAIST-funded Global Singularity Research Program for 2021.

Author contributions

B.-G.P. and K.-J.K. planned and supervised the study. J.-G.C. and JP fabricated the devices and performed the experiment. M.-G.K. helps fabrication of the sample with a gate structure. DK and J.-S.R. help the high-frequency measurement. J.-G.C., JP, K.-J.K., K-J.L., and B.-G.P. analyzed the data and wrote the manuscript.

Competing interests

Authors declare no competing interests.

Data availability

The data that support the findings of this study are available from the corresponding author upon reasonable request.

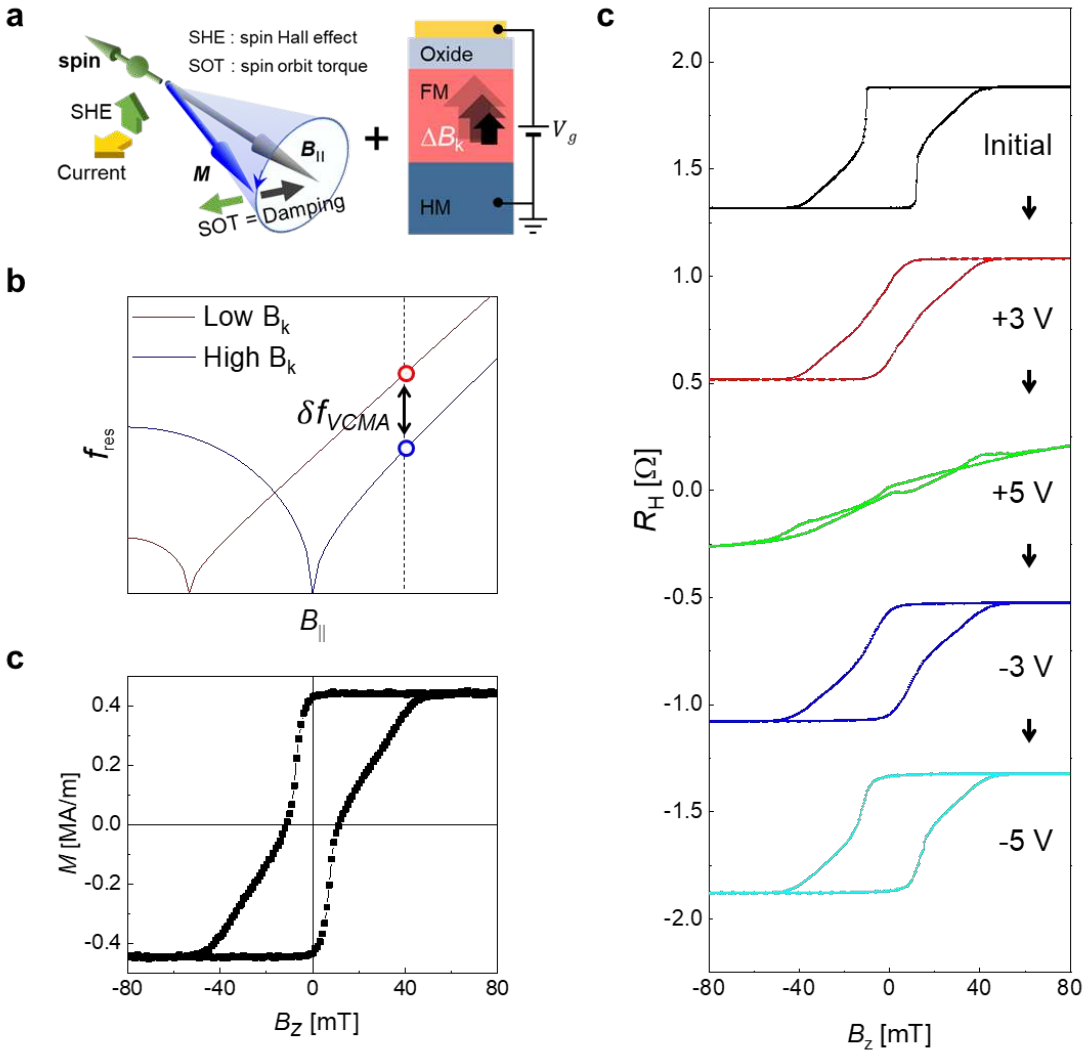

Figure 1. Voltage-controlled perpendicular magnetic anisotropy. a, Schematic illustration of the mechanism of the voltage-driven frequency tuning via voltage-controlled magnetic anisotropy (VCMA). The green and gray arrows represent the directions of spin-orbit torque and damping torque, respectively. **b,** The resonance frequency (f_{res}) as a function of in-plane magnetic field ($B_{||}$) for high PMA (blue) and low PMA (red). **c,** magnetization (M) versus out-of-plane magnetic field (B_{z}) of the Co/Ni film. **d,** Anomalous Hall resistance (R_{H}) curves of the Co/Ni sample for sequentially applied gate voltages of +3V, +5V, -3V, and -5V, respectively.

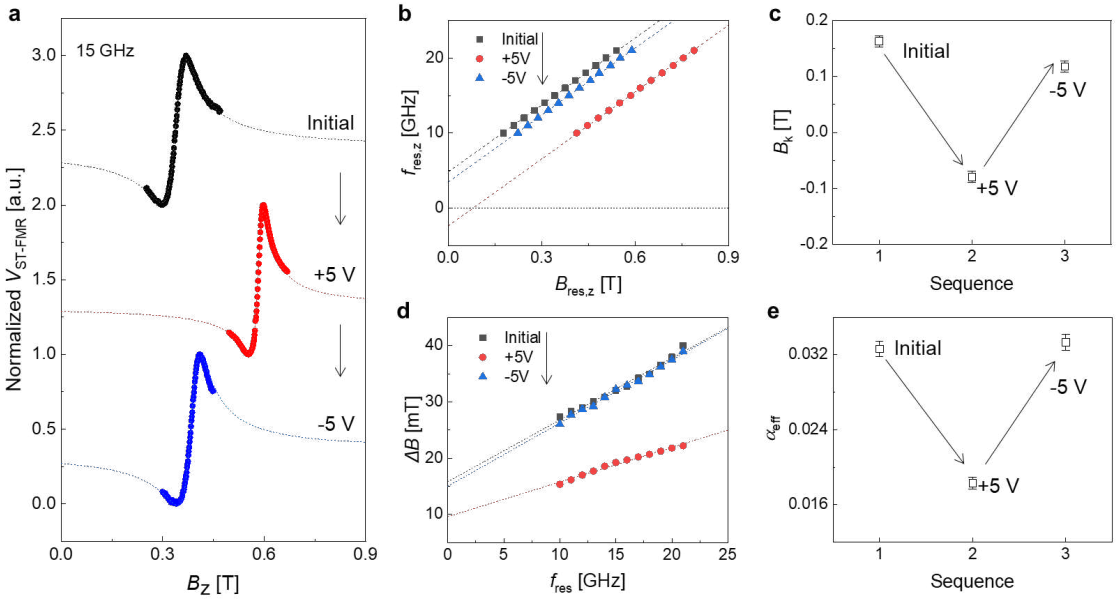

Figure 2. Voltage-dependent ST-FMR spectra. a, ST-FMR spectra of the Co/Ni sample for sequentially applied gate voltages (initial, +5V, and -5V). Here, the microwave frequency is 15 GHz. The dotted lines are the best fits based on Eq. (1). **b,** Resonance frequency ($f_{\mathrm{res,z}}$) as a function of resonance field $B_{\mathrm{res,z}}$ of the sample with different sequentially applied gate voltages. **c,** Variation of perpendicular magnetic anisotropy field (B_{k}) versus sequentially applied gate voltage. **d,** The linewidth of the Lorentzian function (ΔB) as a function of the $f_{\mathrm{res,z}}$ of the sample with sequentially applied gate voltages. **e,** Variation of effective damping constant (α_{eff}) versus sequentially applied gate voltage.

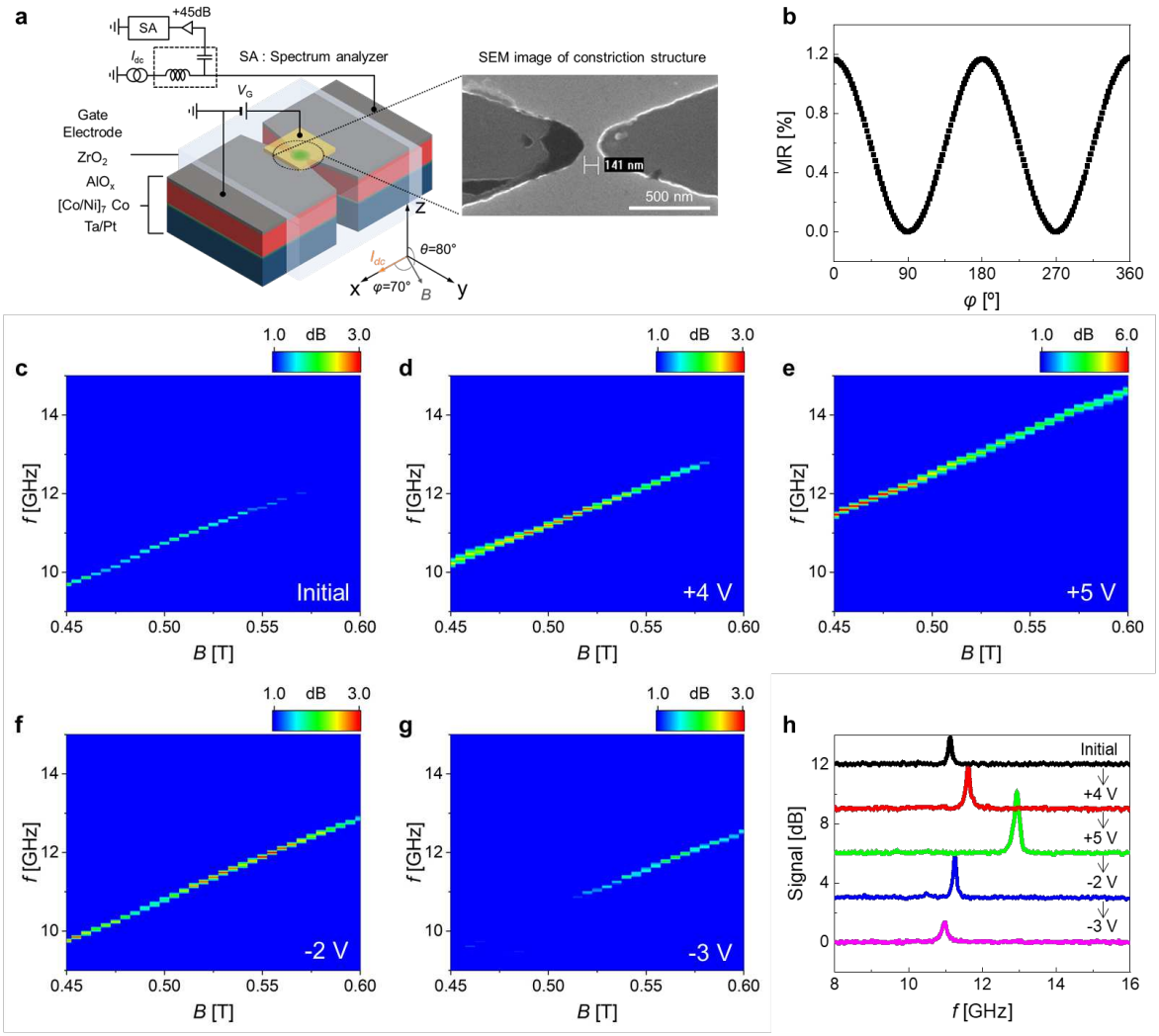

Figure 3. Magnetic field-dependent voltage-driven frequency tuning of SHNO. a, Schematic illustration of the experimental set-up. The inset is a scanning electron microscope image of an SHNO device. **b,** Angle-dependent magnetoresistance (MR) of the Co/Ni sample. **c-g,** Power spectral densities (PSDs) as a function of magnetic field for sequentially applied gate voltages, V_g = 0 V (initial state) (**c**), V_g = +4 V (**d**), V_g = +5 V (**e**), V_g = -2 V (**f**), and V_g = -3 V (**g**). I_{dc}= 2.9 mA. **h,** Auto-oscillation spectra for $B = 0.52$ T with different gate voltages, extracted from Figs. 3c-3g.

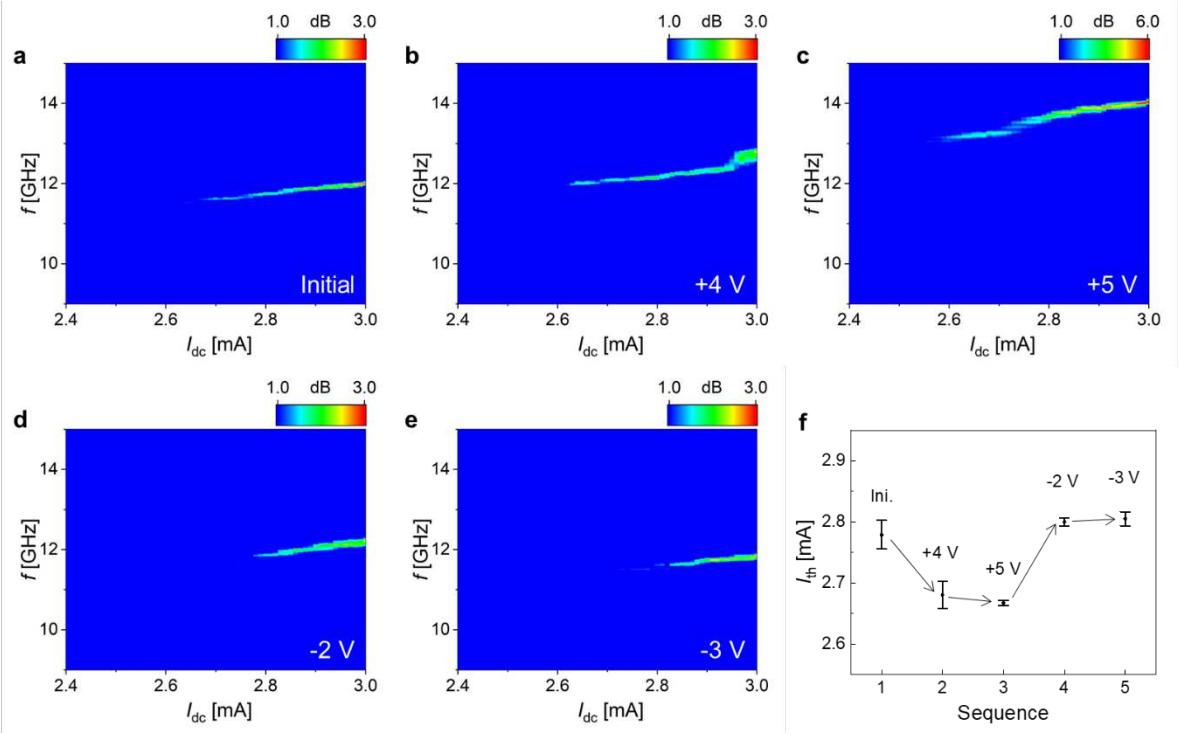

Figure 4. Current-dependent voltage-driven frequency tuning of SHNO. a-e, PSDs as a function of current for sequentially applied gate voltages, V_g = 0 V (initial state) (**a**), V_g = +4 V (**b**), V_g = +5 V (**c**), V_g = -2 V (**d**), and V_g = -3 V (**e**). B = 0.52 T. **f,** Threshold current, I_{th}, according to the sequentially applied gate voltages, extracted from Figs. 4a-4e.

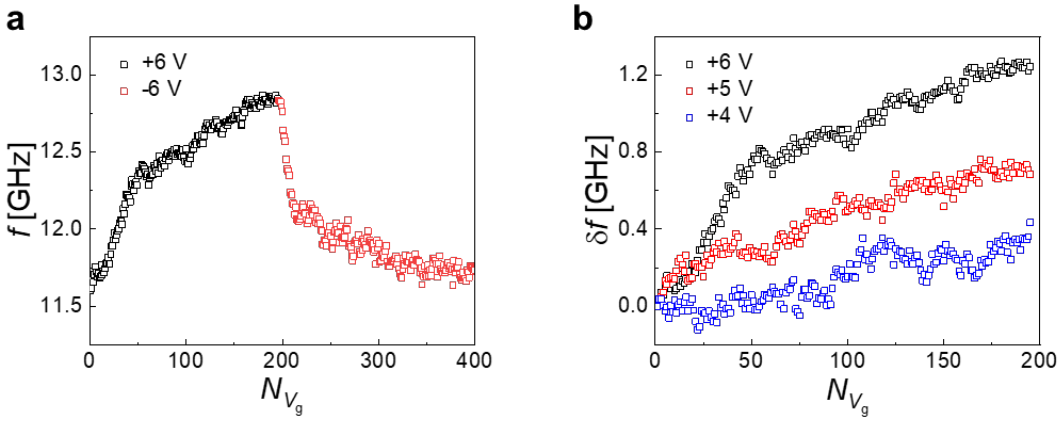

Figure 5. Cumulative frequency control via repetitive gate voltage pulses. a, The auto oscillation frequency of the SHNO versus the number of positive (black) and negative (red) gate voltage pulses (N_{V_g}). **b,** Voltage-driven cumulative frequency change (δf) versus N_{V_g} for different gate voltages.

Supplementary Files

This is a list of supplementary files associated with this preprint. Click to download.

- SIfinal.docx